JM PAPERS

Unsteady drag force on an immersed sphere oscillating near a wall

Zaicheng Zhang[1], **Vincent Bertin**[2], **Martin H. Essink**[2], **Hao Zhang**[1],
Nicolas Fares[1], **Zaiyi Shen**[3], **Thomas Bickel**[1], **Thomas Salez**[1,†] **and**
Abdelhamid Maali[1,†]

[1]Univ. Bordeaux, CNRS, LOMA, UMR 5798, 33405 Talence, France

[2]Physics of Fluids Group and Max Planck Center for Complex Fluid Dynamics, Department of Science
and Technology, and J.M. Burgers Center for Fluid Dynamics, University of Twente, 7500, Enschede,
The Netherlands

[3]State Key Laboratory for Turbulence and Complex Systems, Department of Mechanics and Engineering
Science, College of Engineering, Peking University, Beijing 100871, PR China

The unsteady hydrodynamic drag exerted on an oscillating sphere near a planar wall is
addressed experimentally, theoretically and numerically. The experiments are performed
by using colloidal-probe atomic force microscopy in thermal noise mode. The resonance
frequencies and quality factors are extracted from the measurement of the power spectrum
density of the probe oscillation for a broad range of gap distances and Womersley numbers.
The shift in the resonance frequency of the colloidal probe as the probe goes close
to a solid wall infers the wall-induced variations of the effective mass of the probe.
Interestingly, a crossover from a positive to a negative shift is observed as the Womersley
number increases. In order to rationalize the results, the confined unsteady Stokes equation
is solved numerically using a finite-element method, as well as asymptotic calculations.
The in-phase and out-of-phase terms of the hydrodynamic drag acting on the sphere are
obtained and agree well with the experimental results. All together, the experimental,
theoretical and numerical results show that the hydrodynamic force felt by an immersed
sphere oscillating near a wall is highly dependent on the Womersley number.

Key words: low-Reynolds-number flows, micro-/nano-fluid dynamics

1. Introduction

The motion of particles in a fluid is one of the central problems in fluid mechanics, across
many scales. The hydrodynamic drag force exerted by the fluid on the particles is the
fundamental quantity that dictates the motion. Applications include the sedimentation of

† Email addresses for correspondence: thomas.salez@cnrs.fr, abdelhamid.maali@u-bordeaux.fr

synthetic entities, the swimming of biological microorganisms (see Wang & Ardekani 2012; Wei *et al.* 2019, 2021; Redaelli *et al.* 2023), blood flows (see Ku 1997), peristaltic pumping (see Shapiro, Jaffrin & Weinberg 1969), microfluidic flows (see Dincau, Dressaire & Sauret 2020) and Brownian motion at short times (see Felderhof 2005; Mo & Raizen 2019). At small Reynolds number, while the steady, bulk, Stokes drag force exerted on a translating sphere is well known, addressing further the transient contributions is more intricate – even though the implications of such effects are potentially numerous.

For an isolated spherical particle with radius R translating in a viscous liquid at velocity V, the bulk drag force F at small Reynolds number is given by the Basset–Boussinesq–Oseen (BBO) expression (see Basset 1888; Gatignol 1983; Maxey & Riley 1983; Lovalenti & Brady 1993; Landau & Lifshitz 1987)

$$F = -6\pi\eta R V - 6R^2\sqrt{\pi\rho\eta}\int_{-\infty}^{t}\frac{1}{\sqrt{t-\tau}}\frac{\mathrm{d}V}{\mathrm{d}\tau}\,\mathrm{d}\tau - \frac{2\pi\rho R^3}{3}\frac{\mathrm{d}V}{\mathrm{d}t}, \qquad (1.1)$$

where ρ and η are the density and dynamic viscosity of the viscous liquid, respectively. The right-hand side of this equation includes three terms successively: a Stokes viscous force, a Basset memory term, and an added-mass term. The Basset force originates from the diffusive nature of vorticity within the unsteady Stokes equation, and the added-mass force can be interpreted as an inertial effect due to the displaced fluid mass. Equation (1.1) provides a good description of particle dynamics in a large variety of particle-laden and multi-phase flows, as long as the particle Reynolds number is small (see Balachandar & Eaton 2010).

Nevertheless, the effect of nearby solid boundaries on the unsteady drag is still an open question. The canonical situation is that of an immersed sphere oscillating near a planar rigid surface. Some asymptotic expressions of the drag in the large-distance limit have been derived recently, by using a point-particle approximation together with the method of images (Felderhof 2005, 2012; Simha, Mo & Morrison 2018), or by using low- or high-frequency expansions of the unsteady Stokes equations (Fouxon & Leshansky 2018). However, theoretical descriptions of the confined limit, i.e. where the sphere is in close proximity to the surface, are scarce. We thus aim here to investigate the unsteady drag, in the full spatial range from bulk to confinement, by combining numerical simulations, asymptotic calculations and colloidal-probe atomic force microscopy (AFM) experiments.

The AFM colloidal-probe methods and their surface force apparatus analogues were first introduced in the 1990s in order to measure molecular (e.g. electrostatic or van der Waals) interactions between surfaces (see Butt 1991; Ducker, Senden & Pashley 1991; Butt, Cappella & Kappl 2005). Recently, these methods have been extended and used to study flow under micro-to-nanometric confinement, e.g. near soft (see Leroy & Charlaix 2011; Leroy *et al.* 2012; Villey *et al.* 2013; Guan *et al.* 2017; Zhang *et al.* 2022) or capillary interfaces (see Manor *et al.* 2008; Vakarelski *et al.* 2010; Manica, Klaseboer & Chan 2016; Maali *et al.* 2017; Wang *et al.* 2018; Bertin *et al.* 2021), using complex fluids (see Comtet *et al.* 2017*a*,*b*, 2019), or to measure the friction at solid–liquid interfaces (see Cottin-Bizonne *et al.* 2003; Maali, Cohen-Bouhacina & Kellay 2008; Cross *et al.* 2018), and electrohydrodynamic effects (see Liu *et al.* 2015, 2018; Zhao *et al.* 2020; Rodríguez Matus *et al.* 2022). More specifically, for dynamic colloidal AFM measurements, a micron-size spherical colloidal probe is placed in a viscous fluid, in the vicinity of a surface, with a sphere–wall distance D. Then the probe is driven to oscillate without direct contact, via either acoustic excitation or thermal noise. The force exerted on the sphere is inferred from the colloidal motion, through the cantilever's deflection, which allows us to extract specific information on the confined surfaces or fluid properties. We point out

that other experimental techniques were used to probe the bulk streaming flow around an oscillating sphere at finite Reynolds numbers, like particle visualization techniques (Kotas, Yoda & Rogers 2007; Otto, Riegler & Voth 2008) and optical tweezers (Bruot *et al.* 2021).

If the typical angular frequency of the flow is ω, then the vorticity diffuses on a typical distance $\delta \sim \sqrt{\eta/(\rho\omega)}$ called the viscous penetration length. The dynamic force measurements are usually restricted to low Reynolds numbers and low probing frequencies, and to the confined regime where $D \ll R$. In such a case, the penetration length is large, the flow is located mainly in the confined fluid layer, it is purely viscous and quasi-steady, and the lubrication theory holds (see Reynolds 1886; Leroy & Charlaix 2011). Consequently, in all the above examples, the fluid inertial effects are disregarded in the analysis of the measured hydrodynamic force. This omission is justified by the low Reynolds number, expressed as $Re = \rho\omega AR/\nu$, where A represents the amplitude of the probe's oscillation, and where $\nu = \eta/\rho$ is the kinematic viscosity of the fluid. However, when the colloidal probe oscillates at high frequencies, the penetration depth δ might become comparable to, and even smaller than, the characteristic length scale of the flow. Thus unsteady effects may become important (see Clarke *et al.* 2005), even though *Re* might remain small. The relevant dimensionless number to characterize the crossover to such a regime is the Womersley number $Wo = R\sqrt{\omega/\nu}$, the square of which corresponds to the ratio between the typical diffusion time scale R^2/ν and the period of the oscillation. Unsteady inertial effects should be predominant when it takes more time for the vorticity to diffuse than for the sphere to oscillate, i.e. $Wo > 1$. In such a situation, the hydrodynamic force exerted on the sphere not is only a viscous lubrication drag, but also contains contributions due to the unsteady fluid inertia, which were studied partly in previous works (see El-Kareh 1989; Sader 1998; Benmouna & Johannsmann 2002; Clarke *et al.* 2005; Devailly *et al.* 2020).

The paper is organized as follows. In § 2, we introduce the experimental method of thermal noise AFM and present the typical experimental results. We show that as the distance to the wall is reduced, the resonance frequency increases for low Womersley numbers but decreases for high Womersley numbers. In contrast, the dissipation increases monotonically with decreasing distance for all Womersley numbers. In order to rationalize the results, in § 3, we compute the hydrodynamic drag force in terms of added mass and dissipation, in the asymptotic limit of large distance, and we perform a detailed calculation in the low-Womersley-number limit using the Lorentz reciprocal theorem. Furthermore, a finite-element method is employed to obtain the full numerical solution in all regimes. Finally, the experimental, theoretical and numerical results are summarized and compared in § 4. Mainly, the variation of the resonance frequency is rationalized by the change of the effective mass with distance and Womersley number.

2. Experiments

2.1. *Colloidal-probe AFM set-up*

A schematic of the experimental system is shown in figure 1(*a*). A borosilicate sphere (MOSci Corporation, radius $R = 27 \pm 0.5$ µm) is glued (Epoxy glue, Araldite) to the end of an AFM cantilever (SNL-10, Brukerprobes), and located near a planar mica surface. The cantilever stiffness $k_c = 0.68 \pm 0.05$ N m^{-1} is calibrated using the drainage method proposed by Craig & Neto (2001). The experiments were performed using an AFM (Bruker, Dimension3100) in three different liquids, i.e. water, dodecane and silicone oil, whose densities and dynamic viscosities are 1000 kg m^{-3} and 1 mPa s, 750 kg m^{-3} and 1.34 mPa s, and 930 kg m^{-3} and 9.3 mPa s, respectively, at room temperature.
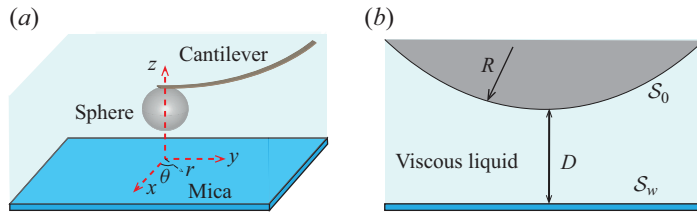
Figure 1. Schematics of the system. A borosilicate sphere with radius R is glued at the end of an AFM cantilever, and fluctuates thermally within a viscous liquid and near a mica substrate, with a distance D between the sphere and the substrate. The sphere and mica surfaces are denoted as S_0 and S_w, respectively.

The sphere–wall distance D was controlled by an integrated stage step motor. Each separation distance was adjusted by displacing the cantilever vertically using the step motor with precision in position <0.1 μm. The zero distance was determined as the point where the deflection signal changed sharply due to the solid–solid contact of the probe with the wall. The cantilever's deflection produced by thermal and hydrodynamic forces acting on the probe was acquired directly using an analogue to digital (A/D) acquisition card (PCI-4462, NI, USA) with sampling frequency 200 kHz. The amplitude of the thermal fluctuation of the probe remained smaller than ~ 1 nm, in all the experiments.

2.2. *Confined thermal dynamics*

The time-dependent position of the spherical probe is denoted $Z(t)$. For a given sphere–wall distance D, the probe dynamics can be modelled by a forced harmonic oscillator (see Jai, Cohen-Bouhacina & Maali 2007; Kiracofe & Raman 2011; Maali & Boisgard 2013), as

$$m_\infty \ddot{Z} + \gamma_\infty \dot{Z} + k_c Z = F_{th} + F_{int}, \tag{2.1}$$

where m_∞ is the effective mass of the probe in the bulk, and γ_∞ is the bulk damping coefficient. These two coefficients correspond to the free dynamics of the probe far from the surface, and can thus be obtained by measuring the resonance properties of the AFM probe in the far field, as shown below. Besides the elastic restoring force by the cantilever of stiffness k_c, and in the absence of conservative forces (e.g. van der Waals or electrostatic forces), the two main forces acting on the sphere along the z direction are the random thermal force F_{th} and the hydrodynamic interaction force with the wall F_{int}. The latter corresponds to the deviation of the hydrodynamic drag with respect to the bulk drag force and depends on the sphere–wall distance.

Taking the Fourier transform of (2.1), we find

$$-m_\infty \omega^2 \tilde{Z} + \mathrm{i}\omega\gamma_\infty \tilde{Z} + k_c \tilde{Z} = \tilde{F}_{th} + \tilde{F}_{int}, \tag{2.2}$$

where $\tilde{f}(\omega) = (1/2\pi) \int_{-\infty}^{\infty} \mathrm{d}t f(t)\, \mathrm{e}^{-\mathrm{i}\omega t}$ is the Fourier transform of the function $f(t)$. The real and imaginary parts of $\tilde{F}_{int}$ correspond to an inertial force and a dissipative force, respectively, that can be recast into

$$\tilde{F}_{int} = m_{int}\omega^2 \tilde{Z} - \mathrm{i}\omega\gamma_{int}\tilde{Z}, \tag{2.3}$$

where m_{int} and γ_{int} are the wall-induced variations of the effective mass and dissipation coefficient. For the sake of simplicity, we neglect in the following the possible frequency dependencies of m_{int} and γ_{int}. With this main assumption, and injecting (2.3) into (2.2),

977 A21-4

the probe's motion follows a thermally forced harmonic oscillator dynamics with spring constant k_c, effective damping coefficient $\gamma \equiv \gamma_\infty + \gamma_{int}$, and effective mass $m \equiv m_\infty + m_{int}$. For the latter problem, one can then derive the one-sided power spectral density $S(\omega) \equiv 2\langle|\tilde{Z}(\omega)|^2\rangle$, as

$$S(\omega) = \frac{2\langle|F_{th}|^2\rangle/(m^2\omega_0^4)}{\left[1 - \left(\dfrac{\omega}{\omega_0}\right)^2\right]^2 + \left(\dfrac{\omega}{\omega_0 Q}\right)^2} = \frac{2k_BT/(\pi Q m\omega_0^3)}{\left[1 - \left(\dfrac{\omega}{\omega_0}\right)^2\right]^2 + \left(\dfrac{\omega}{\omega_0 Q}\right)^2}, \qquad (2.4)$$

where $\langle\cdot\rangle$ denotes the ensemble average, k_BT is the thermal energy, $\omega_0 = \sqrt{k_c/m}$ is the resonance angular frequency, and $Q = m\omega_0/\gamma$ is the quality factor. The second equality in (2.4) is obtained by using the correlator of the noise $\langle F_{th}(t)\,F_{th}(t')\rangle = 2\gamma k_BT\delta_D(t - t')$, where we assumed a white noise through the Dirac distribution δ_D, and where we invoked the fluctuation–dissipation theorem to set the amplitude of the noise. The experimental power spectral densities are fitted by the function (Honig *et al.* 2010; Bowles, Honig & Ducker 2011)

$$S(\omega) = \frac{c_1}{\left[1 - \left(\dfrac{\omega}{\omega_0}\right)^2\right]^2 + \left(\dfrac{\omega}{\omega_0 Q}\right)^2} + c_2, \qquad (2.5)$$

where ω_0 and Q are the key adjustable parameters indicating the position and width of the resonance, and c_1 and c_2 are unimportant extra parameters allowing us to accommodate for potential spurious experimental offset and/or prefactor.

2.3. *Power spectral density*

Figure 2 displays the power spectral densities for probes immersed in dodecane or silicone oil (water was employed as well, but the similar results are not shown here), and for a variety of sphere–wall distances. A well-defined peak can be observed for each spectrum, indicating the fundamental resonance. The resonance properties are well described by the damped harmonic oscillator model above. The largest sphere–wall distance ($D = 100$ µm) corresponds to nearly four times the sphere radius, so that the hydrodynamic interactions between the probe and the wall can be neglected. At such distances, the bulk resonance frequency $\omega_0^\infty = \sqrt{k_c/m_\infty}$ and bulk quality factor $Q_\infty = m_\infty\omega_0^\infty/\gamma_\infty$ are extracted from the fitting procedure, giving respective values 7070 ± 5 Hz and 3.3 ± 0.1 in dodecane, and 5320 ± 5 Hz and 1.3 ± 0.1 in silicone oil. In the more viscous fluid (silicone oil), the resonance is broader since the dissipation is larger, as expected. Also, in both liquids, we observe that the resonance is broader as the sphere gets closer to the hard wall, which indicates that the near-wall dissipation is larger as compared to the bulk situation, as expected too. Besides, and interestingly, the bulk resonance frequency changes significantly from silicone oil to water ($\approx 20\%$ difference in ω_0^∞, which means $\approx 50\%$ difference in effective mass), although the liquid density is similar (less than 10% difference). Hence the effective mass depends on the viscosity of the ambient fluid in a non-trivial way. Moreover, the resonance frequency depends on the sphere–wall distance.

To be quantitative, the fitted values of the resonance frequency ω_0 and the quality factor Q are shown in figure 3 as functions of the normalized separation distance D/R, for the three liquids studied. Intriguingly, we observe an increase of the resonance frequency in silicone oil near the wall as compared to the bulk resonance frequency (figure 3*a*), and a
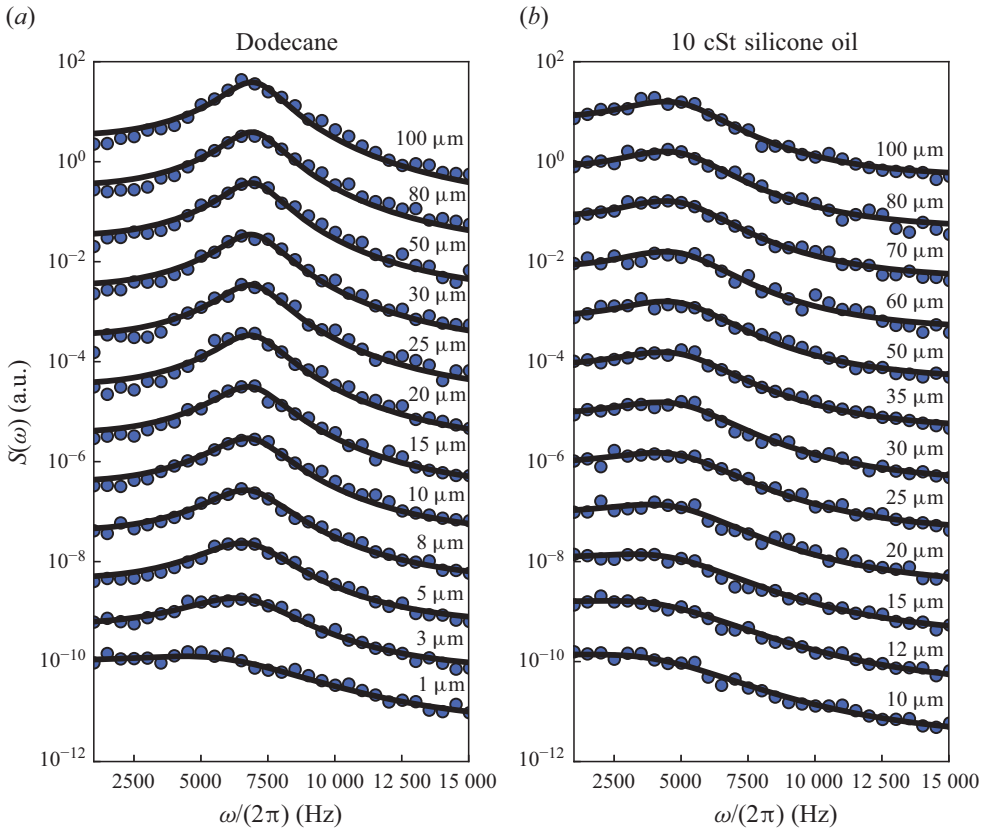
Figure 2. Experimental power spectral densities in arbitrary units (a.u.), for the colloidal probe's vertical position, in (*a*) dodecane and (*b*) silicone oil, for various sphere–wall distances as indicated. The curves are shifted vertically for clarity. The solid lines show the best fits to the damped harmonic oscillator model, using (2.5).

corresponding decrease in dodecane (figure 3*c*) and water (figure 3*e*). We point out that the sphere–wall distances in the present experiments are large enough ($D > 0.5$ μm) so that molecular interactions (e.g. electrostatic or van der Waals forces) can be neglected safely. Therefore, the changes in resonance frequency observed here should result only from hydrodynamic contributions. The next section aims to model this intricate behaviour.

3. Theory

3.1. *Governing equations*

We aim here to calculate the hydrodynamic force exerted on an immersed sphere moving normally near a rigid, flat and immobile wall. The hydrodynamic pressure field is denoted p. The fluid velocity field $\boldsymbol{v}$ satisfies the incompressible Navier–Stokes equations. In order to identify the relevant terms in these, we non-dimensionalize them. Rescaling times by ω^{-1}, lengths by R, velocities by $A\omega$, and pressures by $\eta A\omega/R$, and adding bars for all the dimensionless variables, the dimensionless Navier–Stokes equations read

$$Wo^2\,\partial_{\bar{t}}\bar{\boldsymbol{v}} + Re\,\bar{\boldsymbol{v}}\cdot\bar{\boldsymbol{\nabla}}\bar{\boldsymbol{v}} = -\bar{\boldsymbol{\nabla}}\bar{p} + \bar{\boldsymbol{\nabla}}^2\bar{\boldsymbol{v}}, \quad \bar{\boldsymbol{\nabla}}\cdot\bar{\boldsymbol{v}} = 0, \tag{3.1}$$
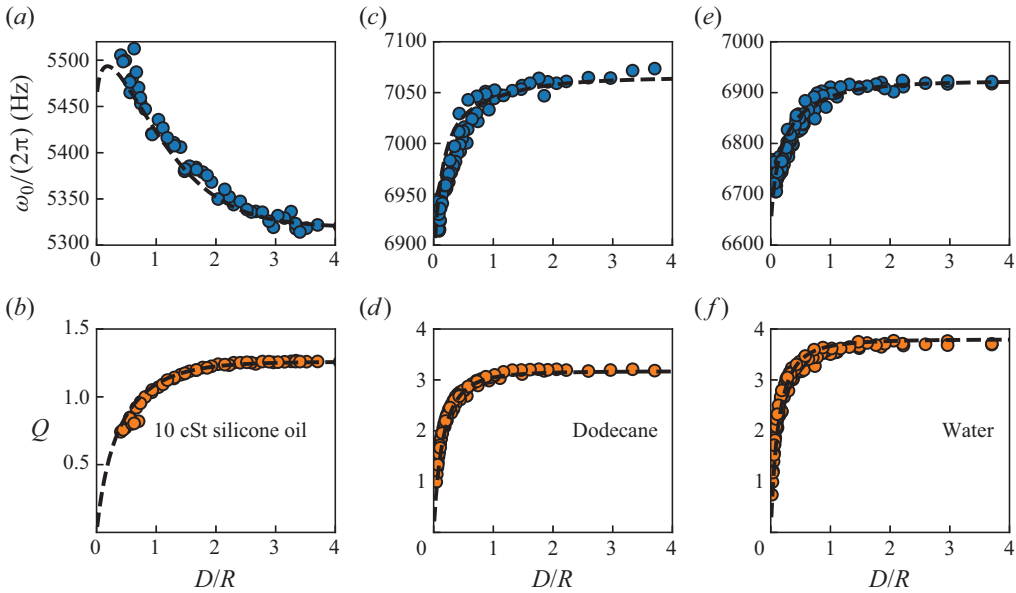
Figure 3. Resonance frequency $\omega_0/(2\pi)$ (blue dots) and quality factor Q (orange dots) of the normal mode of the colloidal AFM probe as a function of dimensionless sphere–wall distance D/R. The dashed lines represent the resonance frequencies and quality factors calculated by (4.3) and (4.4), respectively, without adjustable parameter. (a,b) Results for silicone oil ($\eta = 9.3$ mPa s, $\rho = 930$ kg m^{-3}), with squared Womersley number $Wo^2 = 2.4$. (c,d) Results for dodecane ($\eta = 1.34$ mPa s, $\rho = 750$ kg m^{-3}), with $Wo^2 = 18.1$. (e,f) Results for water ($\eta = 1$ mPa s, $\rho = 1000$ kg m^{-3}), with $Wo^2 = 31.7$.

where $Re = \rho R A \omega / \eta$ is the Reynolds number, and $Wo^2 = R^2 \omega / \nu$ is the squared Womersley number. The amplitude of thermal oscillations in the experiments is nanometric, which implies a relatively small Reynolds number for all accessible frequencies. Therefore, we can neglect the convective term of the incompressible Navier–Stokes equations. Nonetheless, the typical resonance frequency is in the kHz range, such that the squared Womersley number $Wo^2 = R^2 \omega / \nu$ is in the 1–50 range. As a consequence, we expect unsteady inertial effects to be important. The fluid velocity field thus satisfies the unsteady incompressible Stokes equations. Putting back dimensions, the latter reads

$$\rho \, \partial_t \boldsymbol{v} = -\nabla p + \eta \, \nabla^2 \boldsymbol{v}, \quad \nabla \cdot \boldsymbol{v} = 0. \tag{3.2}$$

Without loss of generality, the sphere's position is supposed to oscillate normally to the substrate at frequency ω and with amplitude A, which correspond to a given Fourier mode of the full fluctuation spectrum. Applying the Fourier transform to the unsteady incompressible Stokes equations, we get

$$\mathrm{i}\rho\omega\tilde{\boldsymbol{v}} = -\nabla\tilde{p} + \eta \, \nabla^2 \tilde{\boldsymbol{v}}, \quad \nabla \cdot \tilde{\boldsymbol{v}} = 0. \tag{3.3}$$

A no-slip condition is assumed at both the wall and the sphere surfaces, denoted by $\mathcal{S}_w$ and $\mathcal{S}_0$, respectively (see figure 1b), leading to the following boundary conditions for the fluid velocity field:

$$\tilde{\boldsymbol{v}}(\boldsymbol{r} \in \mathcal{S}_0) = \mathrm{i}\omega A \boldsymbol{e}_z, \quad \tilde{\boldsymbol{v}}(\boldsymbol{r} \in \mathcal{S}_w) = \boldsymbol{0}, \tag{3.4a,b}$$

with $\boldsymbol{e}_z$ the unit vector in the z direction. Here, we suppose that the sphere position is fixed at its average position during one oscillation, as the oscillation amplitude is assumed to

be small. The hydrodynamic drag force applied on the sphere is given by

$$\tilde{F} = \int_{\mathcal{S}_0} \boldsymbol{n} \cdot \tilde{\boldsymbol{\sigma}} \, \mathrm{d}\mathcal{S}_0, \tag{3.5}$$

where $\tilde{\boldsymbol{\sigma}} = -\tilde{p}\boldsymbol{I} + \eta[\nabla\tilde{\boldsymbol{v}} + (\nabla\tilde{\boldsymbol{v}})^{\mathrm{T}}]$ is the fluid stress tensor, and $\boldsymbol{n}$ denotes the unit vector normal to $\mathcal{S}_0$ oriented towards the fluid. To the best of our knowledge, there is no closed-form solution of the problem, in contrast with the steady case (see Brenner 1961). Indeed, the stream function follows the Helmholtz equation (resp. the Laplace equation) associated with the unsteady (resp. steady) Stokes equation. The steady Stokes equation can be solved exactly, using the spectral decomposition of the Laplacian operator in the bispherical coordinate system. Nevertheless, the same methodology cannot be applied to the Helmholtz equation, hence to the unsteady Stokes problem.

By symmetry, the drag force is directed along the z direction, i.e. $\tilde{F} = \tilde{F}_z \boldsymbol{e}_z$. Using dimensional analysis, and assuming that the oscillation amplitude A is much smaller than D, one can show that the drag force $\tilde{F}_z$ normalized by the bulk Stokes reference $-6\mathrm{i}\pi\eta RA\omega$ to form the dimensionless drag force $\tilde{f}_z = \tilde{F}_z/(-6\mathrm{i}\pi\eta RA\omega)$, depends on only two dimensionless parameters: (i) the Womersley number Wo, and (ii) the sphere–wall distance relative to the sphere radius D/R. As a consequence, the dimensionless hydrodynamic interaction force (see § 2.2 and (2.3)) reads

$$\frac{\tilde{F}_{int}}{6\mathrm{i}\pi\eta RA\omega} = \tilde{f}_z(D/R \to \infty, Wo) - \tilde{f}_z(D/R, Wo) = \frac{(m_{int}\omega^2 - \mathrm{i}\omega\gamma_{int})\tilde{Z}}{6\mathrm{i}\pi\eta RA\omega}. \tag{3.6}$$

Although there is no general analytical solution of (3.3) with the boundary conditions (3.4a,b), the hydrodynamic drag force has known asymptotic expressions in certain limits, some of which are given in the next two subsections.

3.2. *Large-distance regime*

In the infinite-distance limit, the force expression reduces to the BBO equation (see (1.1)) for a sphere in an unbounded space, which gives in Fourier space

$$\tilde{F}_z = -6\mathrm{i}\pi\eta RA\omega \left(1 + \sqrt{-\mathrm{i}}\,Wo - \frac{\mathrm{i}\,Wo^2}{9}\right), \quad \text{for } D/R \to \infty. \tag{3.7}$$

The last term of (3.7) corresponds to an inertial force of added mass $2\pi\rho R^3/3$, and the $\sqrt{-\mathrm{i}}\,Wo$ term corresponds to the Basset force, with $\sqrt{-\mathrm{i}} = (1 - i)/\sqrt{2}$. The large-distance asymptotic correction to the added-mass contribution due to a rigid wall has been computed using the potential flow theory, and gives $2\pi\rho R^3\{1 + 3R^3/[8(R + D)^3]\}/3$ (see Lamb 1932). By using a boundary integral formulation of the unsteady incompressible Stokes equations, Fouxon & Leshansky (2018) have generalized the latter result by including the Basset force, to obtain the large-distance asymptotic drag force that reads

$$\tilde{F}_z = -6\mathrm{i}\pi\eta RA\omega \left(1 + \sqrt{-\mathrm{i}}\,Wo - \frac{\mathrm{i}\,Wo^2}{9} + B\,\frac{R^3}{(D + R)^3}\right), \quad \text{for } D/R \gg 1, \tag{3.8}$$

where the numerical prefactor B depends on Wo:

$$B = \frac{1}{4}\left(1 + \sqrt{-\mathrm{i}}\,Wo - \frac{\mathrm{i}\,Wo^2}{3}\right)\left[\frac{1}{3} + \frac{3\mathrm{i}}{2\,Wo^2}\left(1 + \sqrt{-\mathrm{i}}\,Wo - \frac{\mathrm{i}\,Wo^2}{9}\right)\right]. \tag{3.9}$$

3.3. *Small-distance regime*

In the limit of small sphere–wall distance, which is of importance for colloidal-probe experiments, the drag force is usually dominated by viscous effects. The out-of-phase component of the force can be described by lubrication theory (see Batchelor 1967), in which the main contribution to the drag comes from the confined region between the sphere and the wall, which leads to the expression

$$\tilde{F}_z = -\frac{6\mathrm{i}\pi\eta R^2 A\omega}{D}. \tag{3.10}$$

We stress that the in-phase correction to the latter is still unknown in the lubricated limit. It would be interesting to perform asymptotic-matching calculations on the unsteady Stokes equations (see Cox & Brenner 1967) to obtain a self-consistent expression of the effective added-mass in this limit.

3.4. *Low-Womersley-number regime*

As pointed out by Fouxon & Leshansky (2018), in the small-frequency limit, which corresponds to a small Womersley number, the drag force can be expressed in terms of known integrals by using the Lorentz reciprocal theorem (see Masoud & Stone 2019; Fouxon *et al.* 2020). We provide here an alternative derivation of this result.

We introduce the model steady problem of a sphere moving normally to a surface in a viscous fluid, which corresponds to the problem of § 3.1, at zero frequency, i.e.

$$\nabla \cdot \hat{\sigma} = \mathbf{0}, \quad \nabla \cdot \hat{v} = 0, \tag{3.11a,b}$$

with the same boundary conditions

$$\hat{v}(r \in \mathcal{S}_0) = \mathrm{i}\omega A e_z, \quad \hat{v}(r \in \mathcal{S}_w) = \mathbf{0}, \tag{3.12a,b}$$

where $\hat{\sigma}$ and $\hat{v}$ are the fluid stress and velocity fields of the model problem, respectively. Integrating the Lorentz identity $\nabla \cdot (\tilde{\sigma} \cdot \hat{v} - \hat{\sigma} \cdot \tilde{v}) = \mathrm{i}\omega\rho\tilde{v} \cdot \hat{v}$ on the total fluid volume, we obtain

$$(\mathrm{i}\omega A e_z) \cdot \left[\int_{\mathcal{S}_0} \hat{\sigma} \cdot n \, \mathrm{d}\mathcal{S}_0 - \int_{\mathcal{S}_0} \tilde{\sigma} \cdot n \, \mathrm{d}\mathcal{S}_0 \right] = \mathrm{i}\omega\rho \int_{\mathcal{V}} \tilde{v} \cdot \hat{v} \, \mathrm{d}\mathcal{V}, \tag{3.13}$$

where the divergence theorem has been used. Recalling (3.5), we get

$$\tilde{F}_z = \hat{F}_z - \frac{\rho}{A} \int_{\mathcal{V}} \tilde{v} \cdot \hat{v} \, \mathrm{d}\mathcal{V}. \tag{3.14}$$

The force $\hat{F}_z$ and velocity field $\hat{v}$ of the model problem correspond to those derived analytically by Brenner (1961) and Maude (1961) using a modal decomposition. The force of the model problem thus reads

$$\frac{\hat{F}_z}{6\mathrm{i}\pi\eta R\omega A} = \frac{4}{3} \sinh(\alpha) \sum_{n=1}^{\infty} \frac{n(n+1)}{(2n-1)(2n+3)}$$

$$\times \left\{ 1 - \frac{2\sinh[(2n+1)\alpha] + (2n+1)\sinh(2\alpha)}{t[2\sinh((n+\frac{1}{2})\alpha)]^2 - [(2n+1)\sinh(\alpha)]^2} \right\}, \tag{3.15}$$

with $\cosh(\alpha) = 1 + D/R$. Nevertheless, the unsteady velocity field $\tilde{v}$ in (3.14) is still unknown, so the drag force $\tilde{F}_z$ cannot be found exactly.
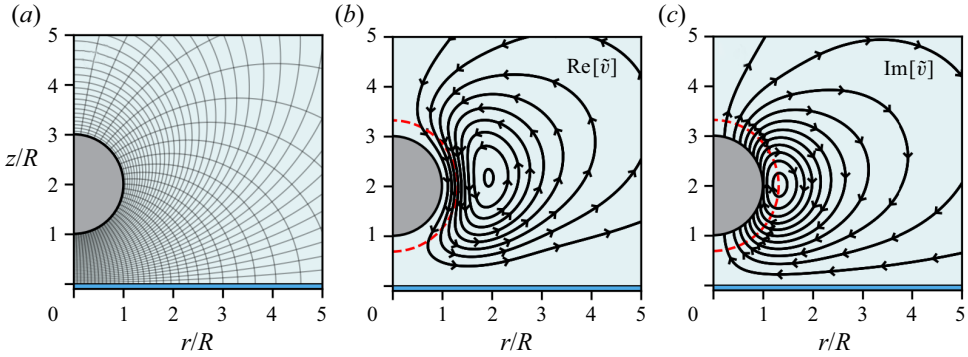
Figure 4. (*a*) Typical mesh used in the finite-element method. (*b*) Streamlines of the in-phase flow field, obtained numerically. (*c*) Streamlines of the out-of-phase flow field, obtained numerically. The squared Womersley number is set to $Wo^2 = 10$, such that $\delta \approx 0.31R$. The red dashed lines indicate a sphere of radius $R + \delta$.

Analytical progress can be made in the low-Wo regime, where the unsteady velocity field can be approximated by the steady solution with $O(Wo^2)$ corrections, as $\tilde{v} = \hat{v}[1 + O(Wo^2)]$. In this limit, at leading order in inertial contributions, the drag force reduces to

$$\tilde{F}_z = \hat{F}_z - \frac{\rho}{A} \int_{\mathcal{V}} \hat{v}^2 \, d\mathcal{V}. \tag{3.16}$$

The volume integral in (3.16) can then be evaluated numerically using the model velocity field provided by Brenner (1961). The volume integral in (3.16) always converges as the velocity field $\hat{v}$ decays exponentially at large radius.

3.5. *Finite-element method*

We complement the previous asymptotic expressions of the drag force with full numerical solutions. Using the open-source finite-element library Nutils (see van Zwieten, van Zwieten & Hoitinga 2022), we solve (3.3). The axisymmetric velocity and pressure fields are defined on a 320×320 element mesh, spaced uniformly on a rectangular domain $[0 \le \tau \le \alpha, \ 0 \le \sigma \le \pi]$. We then use the bipolar coordinate transform

$$r = a \frac{\sin(\sigma)}{\cosh(\tau) - \cos(\sigma)}, \quad z = a \frac{\sinh(\tau)}{\cosh(\tau) - \cos(\sigma)}, \tag{3.17a,b}$$

with $a = R \sinh \alpha$. The resulting mesh, when axisymmetry is considered, spans the entire domain where $r > 0$ and $z > 0$, with the exception of a circular region corresponding to the sphere, as shown in figure 4. On the symmetry axis ($r = 0$), the flow in the radial direction is constrained and the vertical flow is required to be shear-free. At the wall surface ($z = 0$), the velocity field is set to zero. Finally, on the surface of the sphere, the radial and vertical velocity components are set to zero and unity (imaginary part) respectively, following (3.4*a,b*). From the calculated velocity and pressure fields, the total force exerted on the particle can be computed directly using (3.5). Typical flow fields are shown in figures 4(*b,c*).
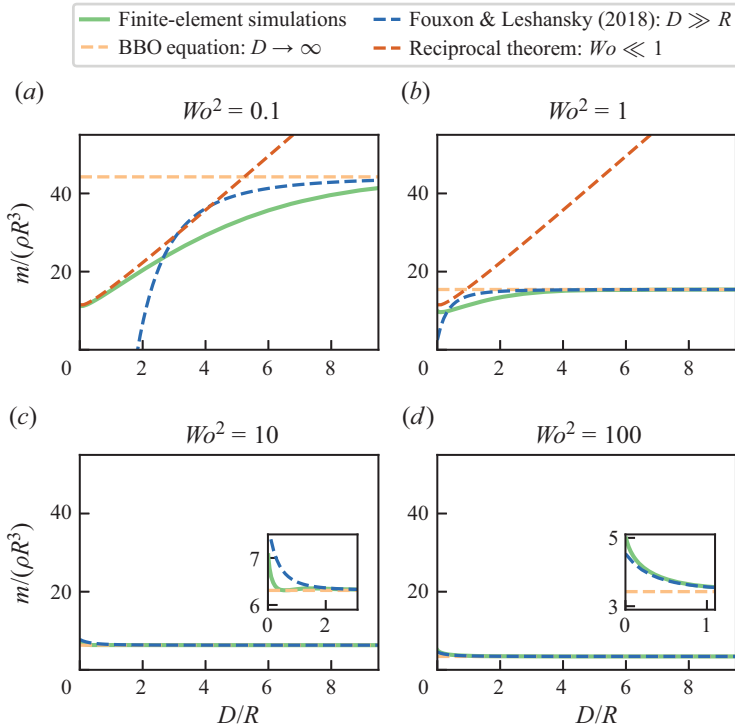
977 A21-10

Figure 5. Real part of the total hydrodynamic force, normalized by the inertial force scale, $\mathrm{Re}[\tilde{F}_z]/(\rho R^3 A \omega^2) = m/(\rho R^3)$, as a function of the normalized sphere–wall distance D/R. The four panels (a–d) correspond to different Womersley numbers, as indicated. The numerical solutions of § 3.5 are shown with solid lines. The bulk BBO force of (3.7) is displayed with light orange dashed lines. The large-distance asymptotic expression of (3.8) is shown with blue dashed lines. The low-Wo expansion of (3.16) is shown with a dark orange dashed line in (a) and (b). The insets in (c) and (d) show zooms near the wall.

4. Results

4.1. *Drag force*

The total hydrodynamic force is decomposed into its in-phase and out-of-phase parts as $\tilde{F}_z = mA\omega^2 - i\gamma A\omega$, and shown in figures 5 and 6 versus the dimensionless sphere–wall distance. First, the BBO force of (3.7) agrees well with the simulation results at large distance, for all Wo. The infinite-distance rescaled effective mass is found to increase with decreasing Womersley number as $\sim 1/Wo$, for $Wo^2 \ll 1$. This effect arises from the Basset term in (3.7). Indeed, invoking the velocity scale $A\omega$, one finds a Basset force that scales as $R^2\sqrt{\rho\eta\omega}\,A\omega \sim \rho R^3 A\omega^2/Wo$. This could rationalize the experimental observations made in figure 2, where the large-distance resonance frequency of the colloidal probe changes in liquids of different viscosities. Conversely, the rescaled damping coefficient increases with increasing Womersley number as Wo, for $Wo^2 \gg 1$ (see figure 6). Here again, this effect originates from the Basset force that also scales as $\eta R A\omega\,Wo$.

Interestingly, the behaviour of the rescaled effective mass with dimensionless distance is not universal. For large Wo, the rescaled effective mass decreases with increasing normalized distance. Furthermore, the large-distance asymptotic expression of (3.8) describes accurately the rescaled effective mass in the $Wo^2 \gg 1$ regime. Indeed, (3.8) is valid as long as the sphere–wall distance exceeds the viscous penetration length,
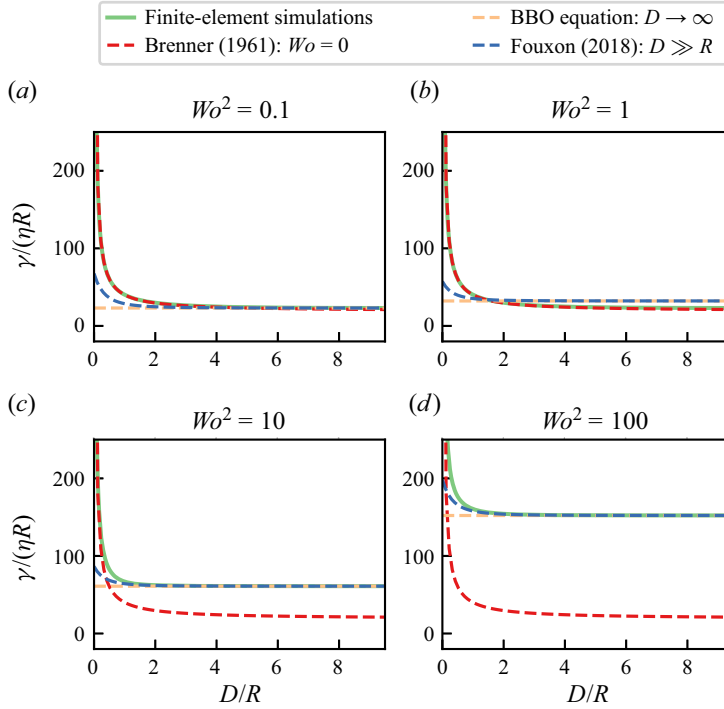
977 A21-11

Figure 6. Opposite of the imaginary part of the total hydrodynamic force, normalized by the viscous force scale, $-\mathrm{Im}[\tilde{F}_z]/(\eta RA\omega) = \gamma/(\eta R)$, as a function of the normalized sphere–wall distance D/R. The four panels (*a–d*) correspond to different Womersley numbers, as indicated. The numerical solutions of §3.5 are shown with solid lines. The bulk BBO force of (3.7) is displayed with light orange dashed lines. The large-distance asymptotic expression of (3.8) is shown with blue dashed lines. The viscous solution of (3.15) is shown with red dashed lines.

i.e. $D \gg \delta = R/Wo$. Near the wall, deviations of the rescaled effective mass from the large-distance asymptotic expression are observed systematically (see insets in figures 5c,d), and are comparable to ~ 1 in magnitude. In sharp contrast, for small *Wo*, the rescaled effective mass decreases with decreasing dimensionless distance. The typical *Wo* value at which the effective mass variation with distance changes sign is given by $Wo^2 \approx 5$. In addition, in the small-*Wo* regime, the numerical solution agrees well with the asymptotic expression (3.16) (see figure 5a) at small dimensionless distances. Eventually, at vanishing sphere–wall distances, the effective mass tends towards a constant value, found numerically to be

$$m \approx 11.45\rho R^3, \quad \text{for } D \ll R \ll \delta. \tag{4.1}$$

Furthermore, an intermediate regime where the rescaled effective mass increases in an affine manner with the dimensionless distance is observed in figure 5(*a*), as predicted by Fouxon & Leshansky (2018):

$$m = \frac{9\pi}{4}\rho R^2(R+D), \quad \text{for } R \ll D \ll \delta. \tag{4.2}$$

The latter asymptotic expression has been obtained by considering the Lorentz correction to the Stokes drag at large distance (see Lorentz 1907; Happel & Brenner 1983).

977 A21-12

The rescaled damping coefficient decreases with increasing dimensionless distance (see figure 6). At low *Wo*, which corresponds to the low-frequency regime, the rescaled damping coefficient is well described at all distances by the steady drag force of (3.15). However, at large *Wo*, we observe a transition from the BBO expression at large distance to the steady drag force at small distance. The typical distance at which the transition occurs is $D \approx \delta$, which is smaller than R. In this regime, the rescaled damping coefficient diverges as $\sim 1/D$, as predicted by lubrication theory (see (3.10)).

4.2. *Comparison of the model with experiments*

We now turn to a comparison of the model with experiments. The resonance properties of the colloidal probe are quantified by the resonance frequency $\omega_0/(2\pi)$ and quality factor Q, as measured by fitting the power spectral density to the harmonic oscillator model (see § 2.3). The resulting values of these two quantities were already shown in figure 3, as functions of the sphere–wall distance, for three different liquids of various kinematic viscosities.

Since the resonance frequency variations are small, typically of the order of 5 % or less of the bulk resonance frequency, we perform a Taylor expansion of the resonance frequency at first order in m_{int}/m_∞:

$$\omega_0 = \sqrt{\frac{k_c}{m_\infty + m_{int}}} \approx \omega_0^\infty \left(1 - \frac{m_{int}}{2m_\infty}\right). \tag{4.3}$$

We then compute the resonance frequency at all distances from the numerical simulations, by using (3.6). The Womersley number is set by using the bulk resonance frequency, through $Wo^2 = R^2 \omega_0^\infty / \nu$. The resulting Wo^2 values are 2.4, 18.1 and 31.7 for silicone oil, dodecane and water, respectively. As shown in figures 3(*a,c,e*), the experimental results agree with the numerical simulation, which confirms that the modification of the resonance frequency of the oscillator originates from the hydrodynamic interactions between the sphere and the wall.

Similarly, we invoke an approximate expression of the quality factor:

$$Q = \frac{Q_\infty}{\dfrac{m_\infty \omega_0^\infty}{m\omega_0}\left(1 + \dfrac{\gamma_{int} Q_\infty \omega_0^\infty}{k_c}\right)} \approx \frac{Q_\infty}{\left(1 + \dfrac{\gamma_{int} Q_\infty \omega_0^\infty}{k_c}\right)}. \tag{4.4}$$

We then compute the quality factor at all distances from the numerical simulations, by using (3.6), and setting the same *Wo* values as given above. As shown in figures 3(*b,d,f*), the experimental results agree with the numerical simulation, confirming that the decrease of the quality factor is essentially due to the increase of the viscous Stokes drag as the sphere–wall distance is reduced.

5. Conclusion

We investigated the hydrodynamic force exerted on an immersed sphere oscillating normally to a rigid planar wall, by using a combination of colloidal-probe AFM experiments, finite-element simulations and asymptotic calculations. The in-phase and out-of-phase components of the hydrodynamic force are obtained from the measurements of the resonance frequency and damping of the thermal motion of the probe for various sphere–wall distances. A shift in the resonance frequency of the probe was observed

with decreasing sphere–wall distance, revealing a striking wall-induced unsteady effect: the resonance frequency was found to increase with decreasing sphere–wall distance in viscous liquids, whereas the opposite trend was observed in low-viscosity liquids such as water. By solving the unsteady incompressible Stokes equations numerically, the hydrodynamic force was computed at all distances. The added mass and dissipation increase due to the presence of the wall were then extracted and compared to their experimental counterparts – with excellent agreement. In addition, at large distance, we recovered the analytical expression derived by Fouxon & Leshansky (2018). Besides, in the low-Womersley-number limit, the hydrodynamic force could be expressed in a simple integral form using the Lorentz reciprocal theorem, which was validated by the numerical simulations. Beneath the fundamental interest for confined or interfacial fluid dynamics, the present results might be of practical importance for colloidal experiments, because they clarify the hydrodynamic drag acting on a spherical particle near a wall. Essentially, our findings highlight the crucial but sometimes overlooked role played by unsteady fluid inertia in a low-Reynolds-number flow.

Declaration of interests. The authors report no conflict of interest.

Author ORCIDs.

Zaicheng Zhang https://orcid.org/0000-0001-7472-1597;

Vincent Bertin https://orcid.org/0000-0002-3139-8846;

Martin H. Essink https://orcid.org/0000-0003-0493-5164;

Nicolas Fares https://orcid.org/0000-0002-8351-6824;

Thomas Bickel https://orcid.org/0000-0003-0987-7629;

Thomas Salez https://orcid.org/0000-0001-6111-8721;

Abdelhamid Maali https://orcid.org/0000-0002-9459-6081.

REFERENCES

BALACHANDAR, S. & EATON, J.K. 2010 Turbulent dispersed multiphase flow. *Annu. Rev. Fluid Mech.* **42**, 111–133.

BASSET, A.B. 1888 *A Treatise on Hydrodynamics,* vol. 2. Deighton, Bell and Co.

BATCHELOR, G.K. 1967 *An Introduction to Fluid Dynamics*. Cambridge University Press.

BENMOUNA, F. & JOHANNSMANN, D. 2002 Hydrodynamic interaction of AFM cantilevers with solid walls: an investigation based on AFM noise analysis. *Eur. Phys. J.* E **9**, 435–441.

BERTIN, V., ZHANG, Z., BOISGARD, R., GRAUBY-HEYWANG, C., RAPHAËL, E., SALEZ, T. & MAALI, A. 2021 Contactless rheology of finite-size air–water interfaces. *Phys. Rev. Res.* **3** (3), L032007.

BOWLES, A.P., HONIG, C.D.F. & DUCKER, W.A. 2011 No-slip boundary condition for weak solid–liquid interactions. *J. Phys. Chem.* C **115** (17), 8613–8621.

BRENNER, H. 1961 The slow motion of a sphere through a viscous fluid towards a plane surface. *Chem. Engng Sci.* **16** (3–4), 242–251.

BRUOT, N., CICUTA, P., BLOOMFIELD-GADÊLHA, H., GOLDSTEIN, R.E., KOTAR, J., LAUGA, E. & NADAL, F. 2021 Direct measurement of unsteady microscale stokes flow using optically driven microspheres. *Phys. Rev. Fluids* **6** (5), 053102.

BUTT, H.-J. 1991 Measuring electrostatic, van der Waals, and hydration forces in electrolyte solutions with an atomic force microscope. *Biophys. J.* **60** (6), 1438–1444.

BUTT, H.-J., CAPPELLA, B. & KAPPL, M. 2005 Force measurements with the atomic force microscope: technique, interpretation and applications. *Surf. Sci. Rep.* **59** (1–6), 1–152.

CLARKE, R.J., COX, S.M., WILLIAMS, P.M. & JENSEN, O.E. 2005 The drag on a microcantilever oscillating near a wall. *J. Fluid Mech.* **545**, 397–426.

COMTET, J., CHATTÉ, G., NIGUES, A., BOCQUET, L., SIRIA, A. & COLIN, A. 2017a Pairwise frictional profile between particles determines discontinuous shear thickening transition in non-colloidal suspensions. *Nat. Commun.* **8** (1), 15633.

COMTET, J., LAINÉ, A., NIGUES, A., BOCQUET, L. & SIRIA, A. 2019 Atomic rheology of gold nanojunctions. *Nature* **569** (7756), 393–397.

COMTET, J., NIGUÈS, A., KAISER, V., COASNE, B., BOCQUET, L. & SIRIA, A. 2017b Nanoscale capillary freezing of ionic liquids confined between metallic interfaces and the role of electronic screening. *Nat. Mater.* **16** (6), 634–639.

COTTIN-BIZONNE, C., BARRAT, J.-L., BOCQUET, L. & CHARLAIX, E. 2003 Low-friction flows of liquid at nanopatterned interfaces. *Nat. Mater.* **2** (4), 237–240.

COX, R.G. & BRENNER, H. 1967 The slow motion of a sphere through a viscous fluid towards a plane surface – II. Small gap widths, including inertial effects. *Chem. Engng Sci.* **22** (12), 1753–1777.

CRAIG, V.S.J. & NETO, C. 2001 In situ calibration of colloid probe cantilevers in force microscopy: hydrodynamic drag on a sphere approaching a wall. *Langmuir* **17** (19), 6018–6022.

CROSS, B., BARRAUD, C., PICARD, C., LÉGER, L., RESTAGNO, F. & CHARLAIX, É. 2018 Wall slip of complex fluids: interfacial friction versus slip length. *Phys. Rev. Fluids* **3** (6), 062001.

DEVAILLY, C., BOURIAT, P., DICHARRY, C., RISSO, F., ONDARÇUHU, T. & TORDJEMAN, P. 2020 Long-range hydrodynamic forces in liquid FM-AFM. *Nanotechnology* **31** (45), 455501.

DINCAU, B., DRESSAIRE, E. & SAURET, A. 2020 Pulsatile flow in microfluidic systems. *Small* **16** (9), 1904032.

DUCKER, W.A., SENDEN, T.J. & PASHLEY, R.M. 1991 Direct measurement of colloidal forces using an atomic force microscope. *Nature* **353** (6341), 239–241.

EL-KAREH, A.W. 1989 I. On a new constitutive equation for non-Newtonian fluids II. Brownian motion with fluid–fluid interfaces. PhD thesis, California Institute of Technology.

FELDERHOF, B.U. 2005 Effect of the wall on the velocity autocorrelation function and long-time tail of Brownian motion. *J. Phys. Chem.* B **109** (45), 21406–21412.

FELDERHOF, B.U. 2012 Hydrodynamic force on a particle oscillating in a viscous fluid near a wall with dynamic partial-slip boundary condition. *Phys. Rev. E* **85** (4), 046303.

FOUXON, I. & LESHANSKY, A. 2018 Fundamental solution of unsteady Stokes equations and force on an oscillating sphere near a wall. *Phys. Rev. E* **98** (6), 063108.

FOUXON, I., RUBINSTEIN, B., WEINSTEIN, O. & LESHANSKY, A. 2020 Fluid-mediated force on a particle due to an oscillating plate and its effect on deposition measurements by a quartz crystal microbalance. *Phys. Rev. Lett.* **125** (14), 144501.

GATIGNOL, R. 1983 The Faxen formulae for a rigid particle in an unsteady non-uniform Stokes flow. *J. Méc. Théor. Appl.* **2**, 143–60.

GUAN, D., CHARLAIX, E., QI, R.Z. & TONG, P. 2017 Noncontact viscoelastic imaging of living cells using a long-needle atomic force microscope with dual-frequency modulation. *Phys. Rev. Appl.* **8** (4), 044010.

HAPPEL, J. & BRENNER, H. 1983 *Low Reynolds Number Hydrodynamics: with Special Applications to Particulate Media*, vol. 1. Springer Science & Business Media.

HONIG, C.D.F., SADER, J.E., MULVANEY, P. & DUCKER, W.A. 2010 Lubrication forces in air and accommodation coefficient measured by a thermal damping method using an atomic force microscope. *Phys. Rev. E* **81** (5), 056305.

JAI, C., COHEN-BOUHACINA, T. & MAALI, A. 2007 Analytical description of the motion of an acoustic-driven atomic force microscope cantilever in liquid. *Appl. Phys. Lett.* **90** (11), 113512.

KIRACOFE, D. & RAMAN, A. 2011 Quantitative force and dissipation measurements in liquids using piezo-excited atomic force microscopy: a unifying theory. *Nanotechnology* **22** (48), 485502.

KOTAS, C.W., YODA, M. & ROGERS, P.H. 2007 Visualization of steady streaming near oscillating spheroids. *Exp. Fluids* **42** (1), 111–121.

KU, D.N. 1997 Blood flow in arteries. *Annu. Rev. Fluid Mech.* **29** (1), 399–434.

LAMB, H. 1932 *Hydrodynamics*. Cambridge University Press.

LANDAU, L.D. & LIFSHITZ, E.M. 1987 *Fluid Mechanics: Landau and Lifshitz: Course of Theoretical Physics*, vol. 6. Pergamon Press.

LEROY, S. & CHARLAIX, E. 2011 Hydrodynamic interactions for the measurement of thin film elastic properties. *J. Fluid Mech.* **674**, 389–407.

LEROY, S., STEINBERGER, A., COTTIN-BIZONNE, C., RESTAGNO, F., LÉGER, L. & CHARLAIX, E. 2012 Hydrodynamic interaction between a spherical particle and an elastic surface: a gentle probe for soft thin films. *Phys. Rev. Lett.* **108** (26), 264501.

LIU, F., KLAASSEN, A., ZHAO, C., MUGELE, F. & VAN DEN ENDE, D. 2018 Electroviscous dissipation in aqueous electrolyte films with overlapping electric double layers. *J. Phys. Chem.* B **122** (2), 933–946.

LIU, F., ZHAO, C., MUGELE, F. & VAN DEN ENDE, D. 2015 Amplitude modulation atomic force microscopy, is acoustic driving in liquid quantitatively reliable? *Nanotechnology* **26** (38), 385703.

LORENTZ, H.A. 1907 Ein allgemeiner satz, die bewegung einer reibenden flüssigkeit betreffend, nebst einigen anwendungen desselben. *Abh. Theor. Phys.* **1**, 23.

LOVALENTI, P.M. & BRADY, J.F. 1993 The hydrodynamic force on a rigid particle undergoing arbitrary time-dependent motion at small Reynolds number. *J. Fluid Mech.* **256**, 561–605.

MAALI, A. & BOISGARD, R. 2013 Precise damping and stiffness extraction in acoustic driven cantilever in liquid. *J. Appl. Phys.* **114** (14), 144302.

MAALI, A., BOISGARD, R., CHRAIBI, H., ZHANG, Z., KELLAY, H. & WÜRGER, A. 2017 Viscoelastic drag forces and crossover from no-slip to slip boundary conditions for flow near air–water interfaces. *Phys. Rev. Lett.* **118** (8), 084501.

MAALI, A., COHEN-BOUHACINA, T. & KELLAY, H. 2008 Measurement of the slip length of water flow on graphite surface. *Appl. Phys. Lett.* **92** (5), 053101.

MANICA, R., KLASEBOER, E. & CHAN, D.Y.C. 2016 The impact and bounce of air bubbles at a flat fluid interface. *Soft Matter* **12** (13), 3271–3282.

MANOR, O., VAKARELSKI, I.U., TANG, X., O'SHEA, S.J., STEVENS, G.W., GRIESER, F., DAGASTINE, R.R. & CHAN, D.Y.C. 2008 Hydrodynamic boundary conditions and dynamic forces between bubbles and surfaces. *Phys. Rev. Lett.* **101** (2), 024501.

MASOUD, H. & STONE, H.A. 2019 The reciprocal theorem in fluid dynamics and transport phenomena. *J. Fluid Mech.* **879**, P1.

MAUDE, A.D. 1961 End effects in a falling-sphere viscometer. *Br. J. Appl. Phys.* **12** (6), 293.

MAXEY, M.R. & RILEY, J.J. 1983 Equation of motion for a small rigid sphere in a nonuniform flow. *Phys. Fluids* **26** (4), 883–889.

MO, J. & RAIZEN, M.G. 2019 Highly resolved Brownian motion in space and in time. *Annu. Rev. Fluid Mech.* **51**, 403–428.

OTTO, F., RIEGLER, E.K. & VOTH, G.A. 2008 Measurements of the steady streaming flow around oscillating spheres using three dimensional particle tracking velocimetry. *Phys. Fluids* **20** (9), 093304.

REDAELLI, T., CANDELIER, F., MEHADDI, R., ELOY, C. & MEHLIG, B. 2023 Hydrodynamic force on a small squirmer moving with a time-dependent velocity at small Reynolds numbers. *J. Fluid Mech.* **973**, A11.

REYNOLDS, O. 1886 IV. On the theory of lubrication and its application to Mr. Beauchamp tower's experiments, including an experimental determination of the viscosity of olive oil. *Phil. Trans. R. Soc. Lond.* **177**, 157–234.

RODRÍGUEZ MATUS, M., ZHANG, Z., BENRAHLA, Z., MAJEE, A., MAALI, A. & WÜRGER, A. 2022 Electroviscous drag on squeezing motion in sphere–plane geometry. *Phys. Rev.* E **105**, 064606.

SADER, J.E. 1998 Frequency response of cantilever beams immersed in viscous fluids with applications to the atomic force microscope. *J. Appl. Phys.* **84** (1), 64–76.

SHAPIRO, A.H., JAFFRIN, M.Y. & WEINBERG, S.L. 1969 Peristaltic pumping with long wavelengths at low Reynolds number. *J. Fluid Mech.* **37** (4), 799–825.

SIMHA, A., MO, J. & MORRISON, P.J. 2018 Unsteady Stokes flow near boundaries: the point-particle approximation and the method of reflections. *J. Fluid Mech.* **841**, 883–924.

VAKARELSKI, I.U., MANICA, R., TANG, X., O'SHEA, S.J., STEVENS, G.W., GRIESER, F., DAGASTINE, R.R. & CHAN, D.Y.C. 2010 Dynamic interactions between microbubbles in water. *Proc. Natl Acad. Sci.* **107** (25), 11177–11182.

VILLEY, R., MARTINOT, E., COTTIN-BIZONNE, C., PHANER-GOUTORBE, M., LÉGER, L., RESTAGNO, F. & CHARLAIX, E. 2013 Effect of surface elasticity on the rheology of nanometric liquids. *Phys. Rev. Lett.* **111** (21), 215701.

WANG, S. & ARDEKANI, A.M. 2012 Unsteady swimming of small organisms. *J. Fluid Mech.* **702**, 286–297.

WANG, Y., ZENG, B., ALEM, H.T., ZHANG, Z., CHARLAIX, E. & MAALI, A. 2018 Viscocapillary response of gas bubbles probed by thermal noise atomic force measurement. *Langmuir* **34** (4), 1371–1375.

WEI, D., DEHNAVI, P.G., AUBIN-TAM, M.-E. & TAM, D. 2019 Is the zero Reynolds number approximation valid for ciliary flows? *Phys. Rev. Lett.* **122** (12), 124502.

WEI, D., DEHNAVI, P.G., AUBIN-TAM, M.-E. & TAM, D. 2021 Measurements of the unsteady flow field around beating cilia. *J. Fluid Mech.* **915**, A70.

ZHANG, Z., ARSHAD, M., BERTIN, V., ALMOHAMAD, S., RAPHAEL, E., SALEZ, T. & MAALI, A. 2022 Contactless rheology of soft gels over a broad frequency range. *Phys. Rev. Appl.* **17**, 064045.

ZHAO, C., ZHANG, W., VAN DEN ENDE, D. & MUGELE, F. 2020 Electroviscous effects on the squeezing flow of thin electrolyte solution films. *J. Fluid Mech.* **888**, A29.

VAN ZWIETEN, J.S.B., VAN ZWIETEN, G.J. & HOITINGA, W. 2022 Nutils 7.0.